SUPPORTING INFORMATION to

A heterometallic [LnLn'Ln] lanthanide complex as a qubit with embedded quantum error correction

CONTENTS

1. SYNTHESIS

Ligand H_2LA was prepared according to our published procedure.[1] Ligand H_2LB and complex $[CeEr_2(LA)_2(LB)_2(py)(H_2O)_2](NO_3)$ (**1**) were prepared as previously reported.[2]

1.1 $[CeLu_2(LA)_2(LB)_2(py)(H_2O)_2](NO_3)$ (2)

A colorless solution of $Ce(NO_3)_3·6H_2O$ (6.9 mg, 0.016 mmol), $Lu(NO_3)_3·6H_2O$ (15.0 mg, 0.032 mmol) and $CuCl_2·2H_2O$ (2.7 mg, 0.016 mmol) in pyridine (10 mL) was treated dropwise under stirring with a light brown solution of H_2LA (10.2 mg, 0.032 mmol) and H_2LB (14.8 mg, 0.032 mmol) in pyridine (10 mL). The resulting green solution was left under stirring at room temperature for 1 h and layered with hexane. Green crystals of $[Cu(py)_4(NO_3)_2]$ were obtained after one week, together with an orange oil. After one month, the later evolved towards a few large orange crystals of **2**, which were filtrated and manually separated (yields around 15 % were typically obtained). Elemental analysis calcd (found) for **2**$·8H_2O$: C 52.09 (51.92), H 3.04 (2.94), N 3.50 (3.34).

1.2 $[LaEr_2(LA)_2(LB)_2(py)(H_2O)_2](NO_3)$ (3)

Compound **3** was obtained as yellow crystals (yields around 15 % were typically obtained) following the same approach carried out for **2** but using $La(NO_3)_3·6H_2O$ (6.9 mg, 0.016 mmol) and $Er(NO_3)_3·5H_2O$ (13.4 mg, 0.032 mmol) instead of $Ce(NO_3)_3·6H_2O$ and $Lu(NO_3)_3·H_2O$, respectively. MS: m/z = 2047.2 $[LaEr_2(LA)_2(LB)_2]^+$. Elemental analysis calcd (found) for **3**$·1.5py·7H_2O$: C 54.03 (53.79), H 3.61 (3.32), N 3.81 (4.16).

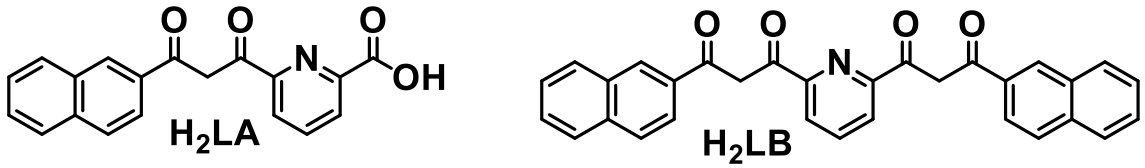

Figure S1. Representation of ligands H_2LA and H_2LB.

2. STRUCTURAL CHARACTERIZATION

2.1 Elemental Analysis

C, H, N analyses were performed by using a Thermo EA Flash 2000 (Thermo Scientific) analyser at the Centres Científics i Tecnològics from the Universitat de Barcelona (CCiT-UB).

[1] *Eur. J. Inorg. Chem.* **2014**, 6013–6021.
[2] *Chem. Eur. J*. **2019**, *25*, 15228–15232.

2.2 Mass Spectrometry

Positive-ion ESI mass spectrometry experiments were performed by using a LC/MSD-TOF (Agilent Technologies) with a dual source equipped with a lock spray for internal reference introduction, at the Unitat d'Espectrometria de Masses from the Universitat de Barcelona. Experimental parameters: capillary voltage 4 kV, gas temperature 325°C, nebulizing gas pressure 103.42 kPa, drying gas flow 7.0 L min-1 and fragmentor voltage 175- 250 V. Internal reference masses were m/z 121.05087 (purine) or 922.00979 (HP-0921). Crystals of **2** and **3** were dissolved in mixtures of MeOH with the minimal amount of DMSO and introduced into the source by using a HPLC system (Agilent 110) with a mixture of H_2O/CH_3CN (1:1) as the eluent (200 μL min^{-1}). As observed previously for compound **1**, the ionization caused the removal of both pyridine and water ligands from the complexes. Moieties related exclusively to the [LuCeLu] and [ErLaEr] metal distributions, respectively, were observed (Figures S2 and S3). Moreover, no signals for other metallic compositions were detected for any of the samples, thus evidencing not only the realization of these trinuclear heterometallic compounds but also their robustness and exclusiveness in solution.

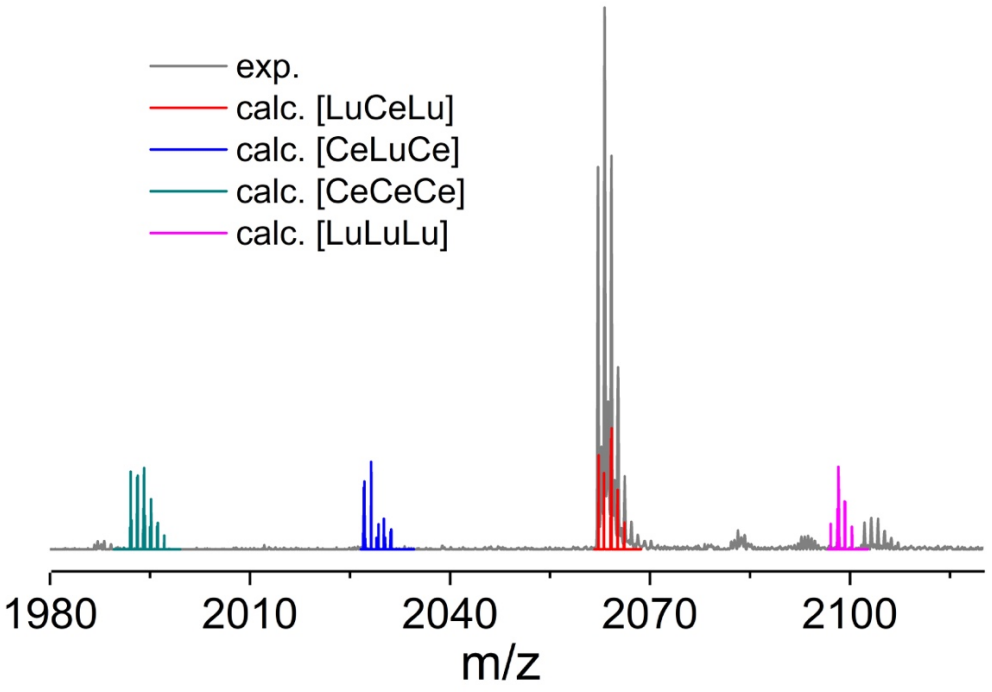

Figure S2. Selected region of the ESI MS spectrum of **2**, emphasizing the $[CeLu_2(LA)_2(LB)_2]^+$ fragment ([LuCeLu], gray line). The calculated signals for [CeCeCe] (green line), [LuCeLu] (red line), [CeLuCe] (blue line), and [LuLuLu] (pink line) fragments are superimposed.

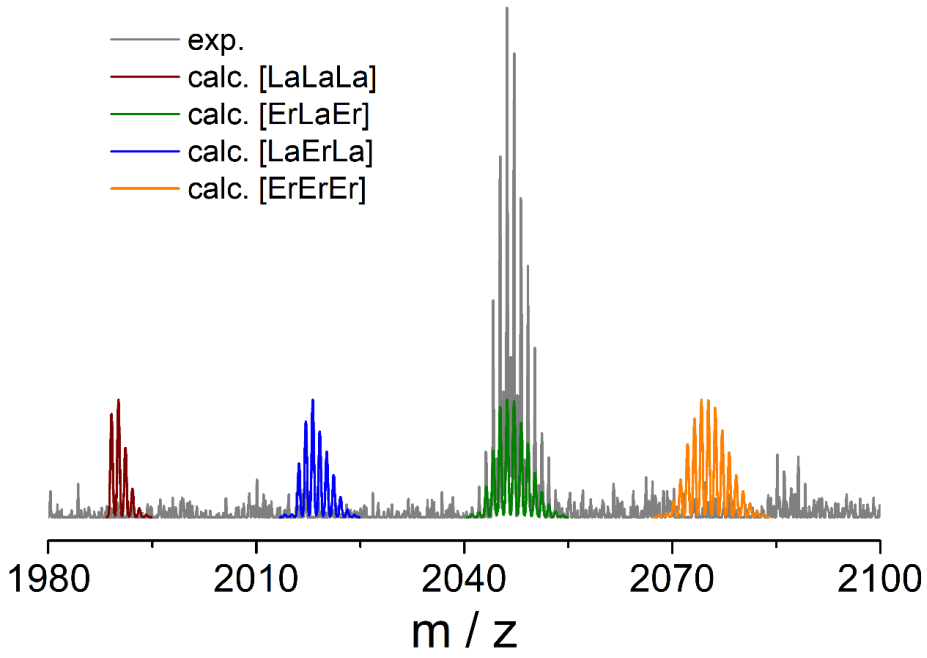

Figure S3. Selected region of the ESI MS spectrum of **3**, emphasizing the $[LaEr_2(LA)_2(LB)_2]^+$ fragment ([ErLaEr], gray line). The calculated signals for [LaLaLa] (red line), [ErLaEr] (green line), [LaErLa] (blue line), and [ErErEr] (orange line) fragments are superimposed.

2.3 Single Crystal X-ray Diffraction (SCXRD)

Data for compound **2** were acquired on a Bruker APEX II QUAZAR diffractometer equipped with a microfocus multilayer monochromator with MoKα radiation (λ = 0.71073 Å) at 100 K. Data reduction and absorption corrections were performed with respectively SAINT and SADABS.[3] Due the very small size of the available crystals of **3**, the use of a synchrotron source was necessary. Thus data for **3** were obtained on a Bruker APEX II CCD diffractometer at the Advanced Light Source beam-line 11.3.1 at Lawrence Berkeley National Laboratory, from a silicon 111 monochromator (λ = 0.77490 Å) at 100 K. Crystal twinning was detected using RLATT[4] and then analyzed with CELL_NOW[4] that found the proper unit cell, twinning law and ascribed reflections to either or both components. Cell refinement and integration were then performed by SAINT as a 2-component twin, keeping the cell of both components identical. TWINABS[4] was used for absorption corrections.

Both structures were solved by intrinsic phasing with SHELXT[5] and refined by full-matrix least-squares on F^2 with SHELXL.[6] In the case of **3**, a void containing only diffuse

[3] SAINT and SADABS, Bruker AXS Inc., Madison, Wisconsin, USA.
[4] G. M. Sheldrick, CELL_NOW and TWINABS, Bruker AXS Inc., Madison, Wisconsin, USA.
[5] G. M. Sheldrick, *Acta Cryst. A*, **2015**, *71*, 3–8.
[6] G. M. Sheldrick, *Acta Cryst. C*, **2015**, *71*, 3–8.

electron density was analyzed and taken into account with PLATON/SQUEEZE,[7] giving an estimated content of five diffuse lattice pyridine molecules, that were included in the formula. All details can be found in CCDC 1998121 and 1998122 that contain the supplementary crystallographic data for this paper. These data can be obtained free of charge from The Cambridge Crystallographic Data Center via https://summary.ccdc.cam.ac.uk/structure-summary-form. Crystallographic and refinement parameters are summarized in Table S1. Hydrogen bond details and the relevant intermolecular Ln···Ln separations are given in Tables S2.

2.4 Powder X-ray Diffraction (PXRD)

Powder X-ray diffraction patterns of **3** were obtained at RT using a D-Max Rigaku, Ru300 diffractometer equipped with Cu rotating anode and graphite monochromator to select the Cu Ka wavelength, through the Servicio General de Apoyo a la Investigación - Universidad de Zaragoza.

To minimize possible loss of crystallinity upon the likely loss of crystallization solvent molecules, fresh crystals of **3** were taken out of their crystallizing mixture with a Pasteur pipette, dropped on a filtration paper and left in air for 5 min to allow for solvent evaporation, and the diffractogram shown in Figure S4 was then acquired *less than 15 minutes* after the crystals were exposed to air.

Although the sample still present some crystallinity, the diffractogram is poor and does not agree with the patterns calculated from the single-crystal structure of **3** at 100 K. This is most likely associated with rapid loss of pyridine lattice molecules and uptake of water from air moist, in agreement with elemental analysis. Measurements performed on samples aged for long periods in air show even poorer crystallinity.

[7] A. L. Spek, *Acta Cryst. C*, **2015**, 71, 9-18.

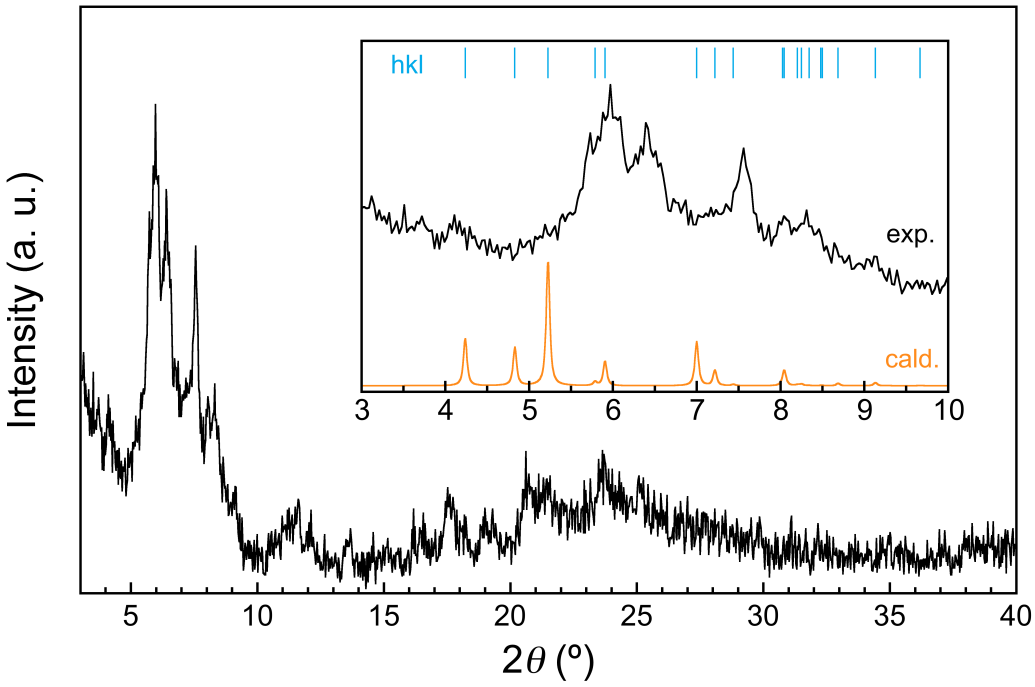

Figure S4. Powder X-ray diffraction patterns at RT for **3**. The inset shows a comparison of the low angles region with the patterns (orange line) and hkl reflections (blue ticks) as calculated from the structure of **3** determined on single-crystals at 100 K.

Table S1. Crystallographic and refinement parameters for the structures of compounds **2** and **3**.

Compound	**2**	**3**
Formula	$C_{160}H_{124}CeLu_2N_{17}O_{21}$	$C_{160}H_{124}Er_2LaN_{17}O_{21}$
FW (g mol^{-1})	3110.81	3094.18
Wavelength (Å)	0.71073	0.7749
T (K)	100	100
Crystal system	triclinic	triclinic
Space group	P–1	P–1
a (Å)	16.4547(15)	16.218(2)
b (Å)	19.5818(18)	19.459(3)
c (Å)	23.333(2)	23.331(3)
α (º)	108.507(5)	108.404(6)
β (º)	108.814(5)	108.158(5)
γ (º)	92.156(5)	91.610(6)
V (Å^3)	6666.0(11)	6572.8(16)
Z	2	2
ρ_{calcd} (g cm^{-3})	1.550	1.563
μ (mm^{-1})	1.885	2.072
Reflections	27409	11510
R_{int}	0.0562	0.0845
Restraints	327	2278
Parameters	1774	1468
S	1.051	1.103
R_1 [I>2σ(I)]	0.0495	0.1080
wR_2 [I>2σ(I)]	0.1229	0.2730
R_1 [all data]	0.0779	0.1661
wR_2 [all data]	0.1436	0.3049
Largest peak / hole (e Å^3)	2.260 / –1.505	4.446 / –1.327

Table S2. Details of hydrogen bonding within the structures of **2** and **3**, together with the relevant shortest intermolecular separation for the paramagnetic lanthanide ion (Ce for **2** and Er for **3**) among pairs of complexes connected through a double hydrogen bond involving O1 and the coordinated water O17.

	D–H (Å)	H···A (Å)	D···A (Å)	D–H···A (º)
2 Ce1···Ce1#1 = 12.931(3) Å				
O17–H17C···O1#1	0.939(19)	1.95(3)	2.707(5)	137(4)
O17–H17D···N1S	0.937(18)	1.83(2)	2.754(7)	167(6)
O18–H18C···N3S	0.893(19)	1.86(2)	2.747(6)	172(6)
O18–H18D···N4S	0.90(2)	1.85(3)	2.713(8)	160(6)
3 Er1···Er#1 = 6.058(6) Å				
O17–H17C···O1#1	0.89(2)	1.93(12)	2.703(18)	144(17)
O17–H17D···N1S	0.90(2)	1.84(3)	2.738(17)	170(13)
O18–H18C···N2S	0.90(2)	1.80(4)	2.60(2)	147(8)
O18–H18D···N5S	0.905(19)	1.81(3)	2.718(18)	176(21)

#1 = 2-x, 1-y, 1-z

Table S3. Average bond distances exhibited by the central Ln' and external Ln ions in the [LnLn'Ln] compounds **1−3**, and differences between these averages, in Å (Ln1 and Ln2 refer to the two crystallographically independent external lanthanide ions). The values for the [HoCeHo] and [YbCeYb] analogues[8] have been included for comparison.

	[HoCeHo]	[YbCeYb]	[ErCeEr] (**1**)	[LuCeLu] (**2**)	[ErLaEr] (**3**)
av. d(Ln'–O)	2.622(30)	2.614(43)	2.622(31)	2.615(32)	2.628(107)
av. d(Ln'–N)	2.790(8)	2.786(13)	2.785(9)	2.787(10)	2.798(35)
av. d(Ln1–O)	2.344(23)	2.301(33)	2.323(23)	2.294(24)	2.322(81)
d(Ln1–N)	2.417(5)	2.387(7)	2.409(5)	2.374(5)	2.401(18)
av. d(Ln2–O)	2.335(23)	2.303(33)	2.325(23)	2.298(24)	2.334(81)
d(Ln2–N)	2.411(5)	2.381(7)	2.400(4)	2.367(5)	2.433(18)
$\Delta O_{Ln'–Ln1}$	0.29	0.31	0.30	0.32	0.31
$\Delta O_{Ln'–Ln2}$	0.29	0.31	0.30	0.32	0.30
$\Delta N_{Ln'–Ln1}$	0.37	0.40	0.38	0.41	0.40
$\Delta N_{Ln'–Ln2}$	0.38	0.41	0.38	0.42	0.37

[8] *Chem. Eur. J*. **2019**, *25*, 15228–15232.

3. DESCRIPTION OF THE MOLECULAR STRUCTURES

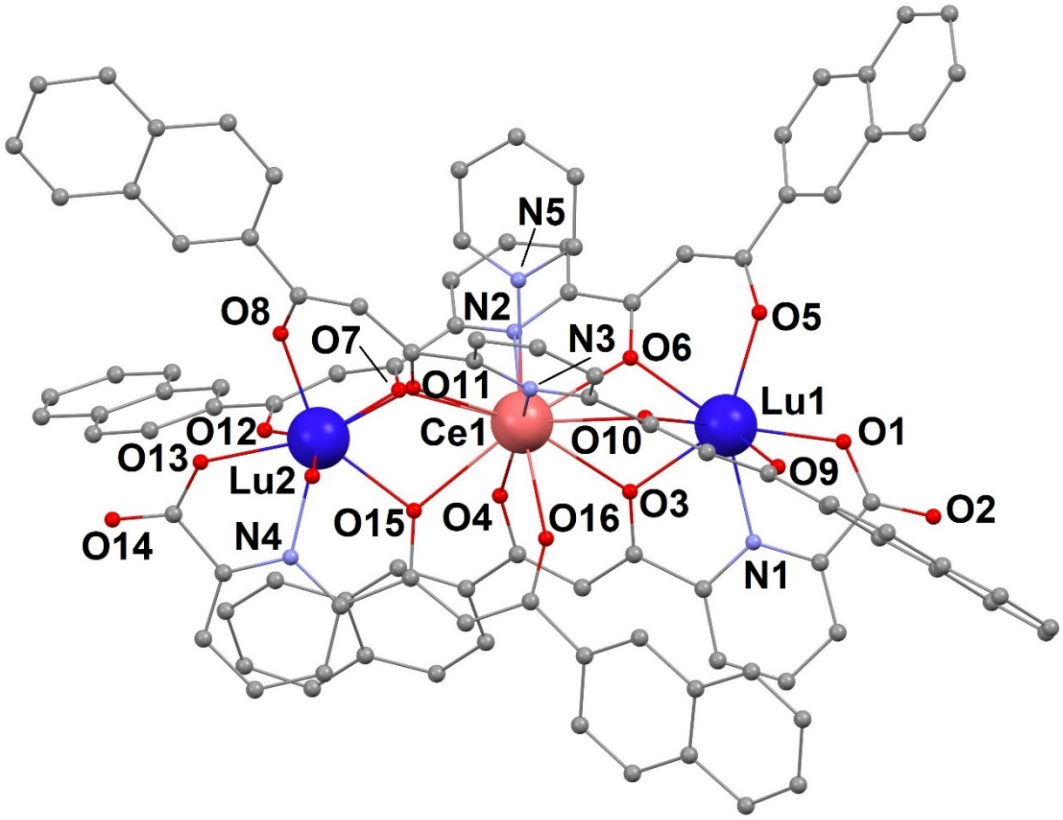

Figure S5. Representation of the molecular structure of the cation of **2**, $[CeLu_2(LA)_2(LB)_2(py)(H_2O)_2]^+$ with heteroatoms labelled. Ce, Lu, C, N and O atoms are shown in salmon, blue, grey, purple and red, respectively. H atoms are omitted for clarity. The cation of **3**, $[LaEr_2(LA)_2(LB)_2(py)(H_2O)_2](NO_3)$ (**3**) is the same, replacing Ce by La and Lu by Er.

Single-crystal X-ray diffraction (SCXRD) provides a detailed description of the structure of the [LuCeLu] (**2**) and [ErLaEr] (**3**) compounds (that of [ErCeEr] (**1**) was previously reported).[9] The three systems are isostructural, crystallizing in the *P*-1 triclinic space group (Table S1). Therefore, the description for [LuCeLu] (**2**) is given here and it will also serve to describe the other two complexes. Metric parameters of the new complexes **2** and **3** are listed in Tables S2 and S3.

The structure of **2** comprises a $[CeLu_2(LA)_2(LB)_2(py)(H_2O)_2]^+$ complex cation (Fig. S5, a NO_3^- anion and eleven pyridine molecules of crystallization, which is the composition of the asymmetric unit. The cation is a heterometallic cluster of three Ln(III) metals arranged linearly in the sequence Lu···Ce···Lu (angle Lu−Ce−Lu, 174.55º). Crystallographically, the heterometallic composition was confirmed at the end of the refinement by replacing Lu by Ce and Ce by Lu, which resulted in large increases of the

[9] *Chem. Eur. J*. **2019**, *25*, 15228–15232.

$R_1/wR_2/S$ parameters, as well as the U_{eq} values, becoming less realistic with distributions other than [LuCeLu]. The metals are held together by two LA^{2-} ligands (following the double deprotonation of H_2LA, Fig. S1) comprising two β-diketonate coordination pockets (O,O) fused to a central dipicolinate-like (O,N,O) coordinating unit. The distal units promote coordination to Ln ions with shorter Ln−O bond distances than the central one, thus, the smaller Lu(III) ions are chelated by the β-diketonate moieties, and Ce(III) is allocated at the central pocket. Two smaller LB^{2-} donors (from H_2LB, Fig. S1) further chelate the metals pairwise, bridging the central Ln(III) ion with one of the distal ions each. Coordination number eight around Lu(III) (O_7N) is completed by one molecule of water, producing a distorted bi-augmented trigonal prism as calculated by continuous-shape measures (CShMs, Table S4). The undecacoordination of Ce(III) (O_9N_3) is achieved with the concourse of one pyridine ligand, and is best described as a capped pentagonal antiprism by CShMs (Table S4).

Metal Allocation Selectivity

As suggested above, the selectivity on the allocation of the different metals in their corresponding positions is determined by their relative ionic radii. The reason is that the central position of the cluster engenders longer Ln−O bonds that in the sides. This is mirrored by the observed parameters listed in Table S3. Since the origin for this difference in bond distances is the scaffold formed by LA^{2-} and LB^{2-} ligands, only the Ln–O distances involving these two donors are considered. This property had been discovered already for the previously reported [LnLn'] family of dinuclear complexes, where a majority of (O,N,O) pockets with respect to (O,O) sites favour larger metal ions. In Table S3, the parameters of the previously reported[10] analogous complexes with metal compositions [HoCeHo], [YbCeYb] and [ErCeEr] (**1**) are included for comparison. In all cases, the central Ln(III) ion (Ce or La) always exhibits longer Ln–O distances than the peripheral ones (Ho, Er, Yb, Lu). Accordingly, the ionic radius of the central ion is larger than that of the external ones; radii of 1.220 and 1.250 Å for Ce(III) and La(III) and of 1.055, 1.040, 1.010 and 0.995 Å for Ho(III), Er(III), Yb(III) and Lu(III), respectively, all if nine-coordinate.[11] The selectivity increases with the value of the parameter ΔO (or ΔN). It is the difference between the average of Ln-O (or Ln-N) bond distances of the central ion and these of the peripheral ones (Table S3). These values (in the range of 0.30-0.32 Å for ΔO, and 0.37-0.42 for ΔN) suggest a strong site selectivity, found to be even larger than observed for the [LnLn'] system.[12] The complexes establish a network of H-bonding and π-π stacking interactions, resulting in intermolecular Ln···Ln distances (Ln = Lu, Er) that are shorter than within the molecules (6.067 and 6.058 Å for **2** and **3**, respectively, Fig S6).

[10] *Chem. Eur. J*. **2019**, *25*, 15228–15232.
[11] *Inorg. Chem.* **2011**, *50*, 4572-4579.
[12] *J. Am. Chem. Soc.* **2014,** *136*, 14215-14222.

Table S4. Continuous-Shape Measures (CShMs) for the coordination geometry of Lu(III)/Er(III) and Ce(III)/La(III) ions in compounds **2** and **3** (coordination number 8 and 11, respectively) with respect to seven reference polyhedra (being 0 a perfect match between the environment of the ion and the ideal polyhedron).[13] Highlighted is the closest polyhedron for each metal. Below is the symmetry and description of each polyhedron.

	CU-8	***SAPR-8***	***TDD-8***	***JGBF-8***	***JBTPR-8***	***BTPR-8***	***JSD-8***
Lu1 (1)	12.43	3.04	2.18	12.75	2.11	1.33	3.84
Lu2 (1)	12.89	3.40	2.16	13.69	2.26	1.47	3.93
Er1 (2)	12.32	3.46	2.15	13.08	2.32	1.36	4.37
Er2 (2)	13.09	3.59	2.47	13.22	2.43	1.63	4.10
	HP-11	***DPY-11***	***EBPY-11***	***JCPPR-11***	***JCPAPR-11***	***JAPPR-11***	***JASPC-11***
Ce (1)	35.58	25.54	19.34	7.42	6.35	11.82	8.31
La (2)	35.46	25.71	19.95	7.39	6.05	11.68	8.02

CU-8	O_h	Cube
SAPR-8	D_{4d}	Square antiprism
TDD-8	D_{2d}	Triangular dodecahedron
JGBF-8	D_{dd}	Johonson gyrobifastigium J26
JBTPR-8	C_{2v}	Biaugmented trigonal prism J50
BTPR-8	C_{2v}	Biaugmented trigonal prism
JSD-8	D_{2d}	Snub diphenoid J84
HP-11	D_{11h}	Hendecagon
DPY-11	C_{10v}	Decagonal pyramid
EBPY-11	D_{9h}	Enneagonal bypyramid
JCPPR-11	C_{5v}	Capped pentagonal prism J9
JCPAPR-11	C_{5v}	Capped pentagonal antiprism J11
JAPPR-11	C_{2v}	Augmented pentagonal prism J52
JASPC-11	C_s	Augmented sphenocorona J87

[13] Chem. Eur. J. 2005, 11, 1479–1494.

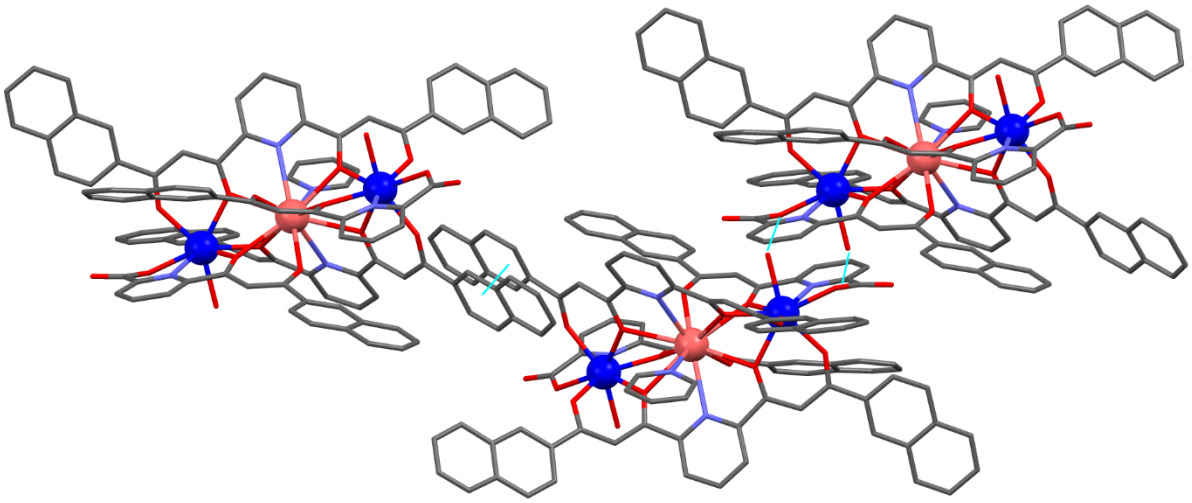

Figure S6. Representation of the crystallographic packing of $[CeLu_2(LA)_2(LB)_2(py)(H_2O)_2]^+$ (cation of **2**), emphasizing the H-bonding and π-π interactions (blue lines). The molecules linked by two hydrogen bonds are related by a crystallographic rotation axis (see matrix in section 4.3). The same pattern is observed for **1** and **3**.

4. PHYSICAL CHARACTERIZATION (magnetization, specific-heat and CW-EPR)

Magnetic measurements.

Magnetic measurements were performed using a Quantum Design SQUID MPMS-XL magnetometer through the Physical Measurements unit of the Servicio de Apoyo a la Investigación-SAI, Universidad de Zaragoza.

All data were corrected for the sample holders and grease contributions, determined empirically as well as for the intrinsic diamagnetism of the sample, estimated using Pascal constants.

Heat capacity experiments

Heat capacity data were measured, down to T = 0.35 K, with a commercial physical property measurement system (PPMS, Physical Measurements unit of the Servicio de Apoyo a la Investigación-SAI, Universidad de Zaragoza) that makes use of the relaxation method. The samples, in powder form, were pressed into pellets and placed onto the calorimeter on top of a thin layer of Apiezon N grease that fixes the sample and improves the thermal contact. The raw data were corrected from the known contributions arising from the empty calorimeter and the grease.

Electron Paramagnetic Resonance experiments.

Continuous wave (cw) EPR measurements were performed with a Bruker Biospin ELEXSYS E-580 spectrometer operating in the X-band. Experiments were performed at T = 6 K on polycrystalline samples of the three compounds (by crushing large single crystal specimens obtained during the reaction). The background signals from the empty cavity and the quartz tubes used as sample holders were measured independently and subtracted from the experimental results. For comparison, cw-EPR measurements were also done on a frozen saturated solution of [ErCeEr] in a 1:1 MeOH/EtOH nondeuterated mixture (approximate concentration between 6 and 15 mM) with a tiny amount of deuterated DMSO to increase the [ErCeEr] solubility. In addition, pulsed Time Domain (TD) measurements were performed at X-band frequencies on the latter solution. In these experiments, the typical widths of the $\pi/2$ and π pulses were 16 ns and 32 ns, respectively. In order to avoid unwanted echoes, a 2-step phase cycle was used in the 2-pulse and inversion recovery experiments. The high-power microwave excitation was obtained by using a TWT amplifier. A dielectric low Q cavity from Bruker was used as resonator.

4.1. χT plots of [LuCeLu] and [ErLaEr]: definition of qubit states

Susceptibility measurements performed on powdered samples (from crushed large single crystals) of **2** and **3**, shown in Fig. S7, indicate that both Ce^{3+} and Er^{3+} can be described at low temperature as effective spin doublets, separated respectively by a gap of 210 and 77 K from the higher excited doublets. These doublets provide therefore a suitable encoding for each of the three qubits. In sections 4.2 to 4.4 below, we focus

on the characterization of the low-lying spin doublets (in [LuCeLu] and in [ErLaEr]) and of the intramolecular spin-spin couplings (in [ErCeEr]).

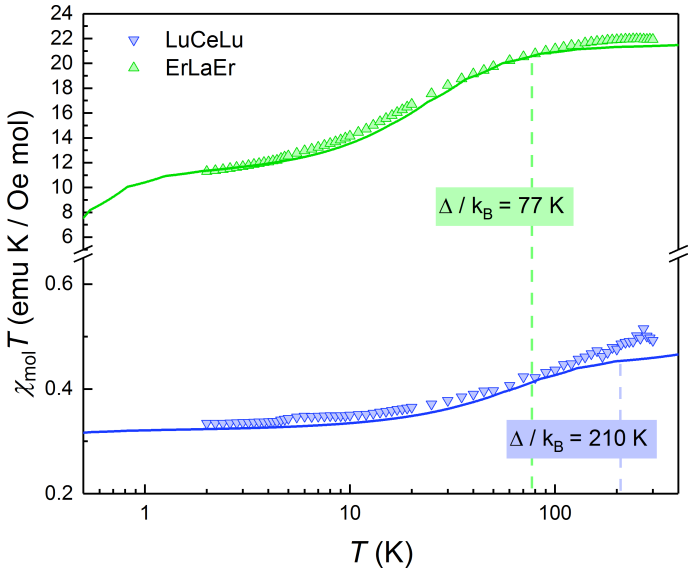

Figure S7 χT plots of **2** (blue) and **3** (green). The increase of χT with T marks the population of excited doublets. The solid lines are least-squares fits with a simplified version[14] of the Van-Vleck susceptibility model that takes into account two spin doublets and that allows estimating the energy gap Δ that separates them. The results show that, liquid Helium temperatures, Ce(III) and Er(III) ions in these molecules behave as two level spin systems.

4.2 Characterization of [LuCeLu]

As reported in the main text (Fig. 2), experimental data for **2** are satisfactorily reproduced by an isotropic model using the effective $\mathbf{g}_{\mathrm{Ce}} = (1.85, 1.85, 1.85)$. The slight deviation between data and simulation in magnetization measurements at high field and low temperature can be fixed by employing an axially anisotropic $\mathbf{g}_{\mathrm{Ce}} = (1.7,1.7,2.2)$. This choice also slightly improves the fit of CW-EPR and specific heat data (see Fig. S8 below).

[14] Bartolomé, E.; Alonso, P. J.; Arauzo, A.; Luzón, J.; Bartolomé, J.; Racles, C.; Turta, C. *Dalton Trans.* **2012**, *41*, 10382−10389.

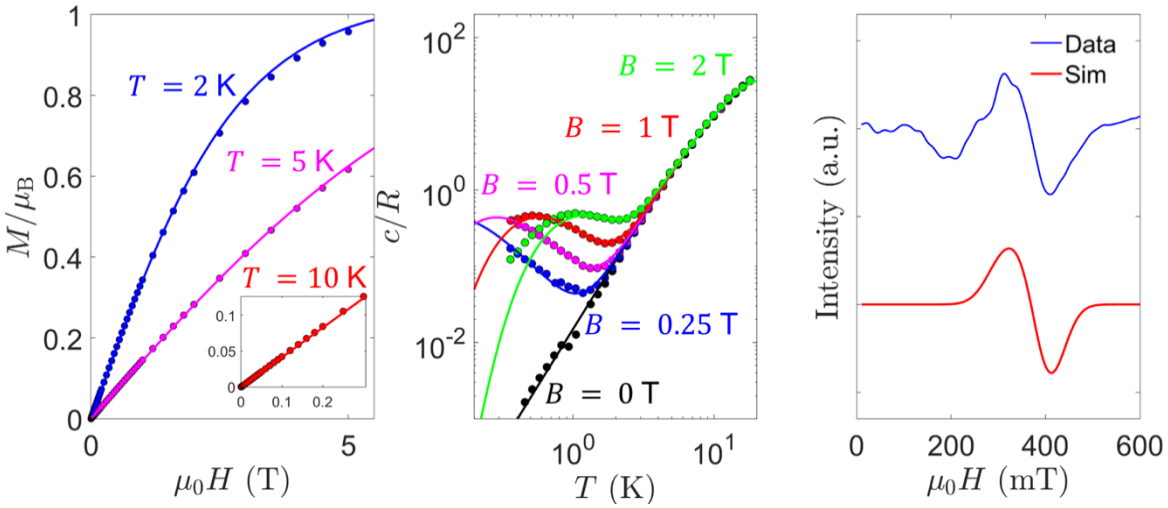

Figure S8. Magnetization as a function of magnetic field on **2** (left): experimental data (circles) and calculation (solid lines) at three different temperatures. Specific heat as a function of temperature on **2** (middle): experimental data (circles) and calculation (solid lines) at five different static field values. CW-EPR data (right) measured on **2** (blue line) together with the spectrum simulated with the Easyspin[15] package for MATLAB (red line).

We finally note that the dip near 200 mT in the EPR spectrum and the background signal above 500 mT correspond with features observed in measurements of the bare quartz tubes, which have likely not been completely corrected, on account of the low signal arising from the sample.

4.3 Characterization of [ErLaEr]

The set of measurements performed on [ErLaEr] (**3**) molecule (Fig. 2, bottom panels, main text) has been well reproduced by using $\mathbf{g}_{\mathrm{Er1}} = (1, 5, 11.5)$. As mentioned in the main text, the two Er ions are practically (even if not exactly) related by the rotation expressed by the following matrix:

$$R = \begin{bmatrix} -0.9980 & 0.0628 & 0.0000 \\ 0.0568 & 0.9030 & -0.4258 \\ -0.0267 & -0.4249 & -0.9048 \end{bmatrix}$$

This represents a rotation of about 25 degrees around an axis close to x followed by two reflections: one across the yz plane and the other across the xy plane. We used this matrix to calculate $\mathbf{g}_{\mathrm{Er2}} = R^{-1}\mathbf{g}_{\mathrm{Er1}}R$, therefore reducing the number of free parameters.

[15] Stoll, S.; Schweiger, A.; *Journal of Magnetic Resonance* **2006**, *178*, 42-55.

Measurements on **3** have been performed on concentrated samples. In this case, a correct interpretation of the experiments must include sizable inter-molecular interactions. Indeed, molecules in the crystal are arranged as shown in Fig. S5, where the two closest Er^{3+} ions belonging to neighboring molecules are only ~ 6 Å apart and hence are characterized by an inter-molecule dipolar interaction comparable to the intra-molecular one. Thus, in our simulations we considered "chains" of four Er^{3+} ions (as sketched in Fig.S4) with nearest-neighbor dipolar interactions (both inter- and intra-molecular).

A Schottky peak in zero-field specific heat measurements indicates a sizeable dipolar $\mathrm{Er}-\mathrm{Er}$ interaction. In the point-dipole approximation, this only depends on $\mathbf{g}_{\mathrm{Er1}}$ and on the known relative position of the two ions, thus allowing us to determine $\mathbf{g}_{\mathrm{Er1}}$. By assuming the largest component of $\mathbf{g}_{\mathrm{Er1}}$ (11.5 ± 0.3) along the Er-Er direction, we obtain a dipolar splitting able to correctly reproduce the zero-field gap in specific heat measurements (Fig. 2, bottom middle panel). The intermediate component of $\mathbf{g}_{\mathrm{Er1}}$ (5.0 ± 0.3) is chosen to fit the features of CW-EPR experimental data around $100-200$ mT. Finally, $g_{\mathrm{Er1,x}} = 1 \pm 1$ is obtained by a combined fit of all experimental data, with a relatively large uncertainty due to the broadening of high-field features in CW-EPR spectra and the consequent difficulty in precisely determine a lower bound. We have also checked that the inclusion of off-diagonal terms in $\mathbf{g}_{\mathrm{Er1}}$ does not improve the fit.

4.4 Characterization of [ErCeEr]

Having fixed $\mathbf{g}_{\mathrm{Ce}}$ and $\mathbf{g}_{\mathrm{Er1}}$, analogous measurements were performed on **1**. We report in the main text a comparison between measurements and simulations, showing a good agreement. Here the only difference from the previous analysis is the inclusion of spin-spin interactions between Ce^{3+} and Er^{3+}. To rule out inter-molecular couplings and focus on the intra-molecular $\mathrm{Ce}-\mathrm{Er}$ interaction, CW-EPR measurements were performed on a diluted sample. The corresponding simulations were carried out with a tailored program, which calculates the integrated spectrum using an energy-fixed peak width[16,17].
We show below some additional specific heat measurements performed on **1** at higher static field values, not reported in the main text for sake of clarity.

[16] Pilbrow, J. R.; *Journal of Magnetic Resonance* **1984** *58*, 186-203
[17] Orton, J. W.; *Electron Paramagnetic Resonance*; Gordon and Breach, (1969).

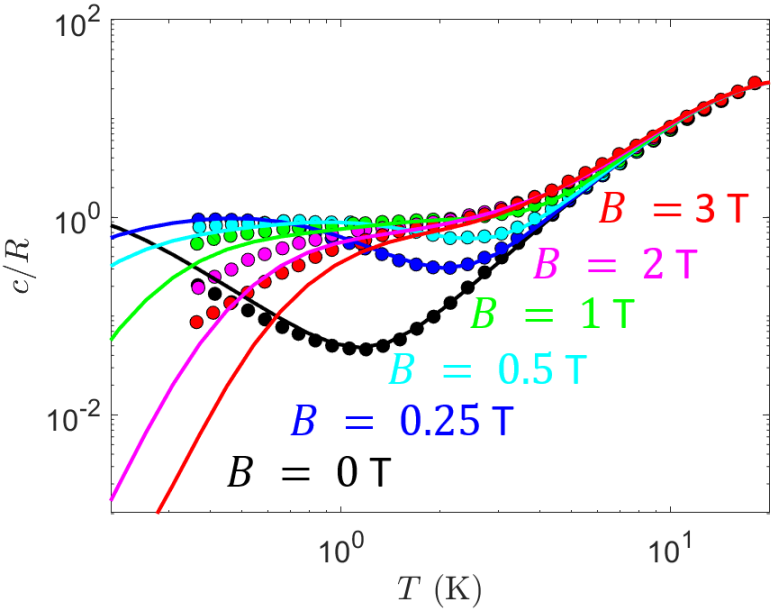

Figure S9. Specific heat vs. temperature on **1**: experimental data (circles) and calculation (solid lines) at six different static field values.

As discussed in the main text, the whole set of experimental data on **1** has been well reproduced by using the Er-Ce dipole-dipole interaction obtained from the **g** tensors determined previously from independent measurements on **2** and **3** analogues. To do this, we have used the point-dipole approximation, which constitutes a safe choice for rare-earth ions characterized by well localized magnetic moments. However, to provide a deeper study of the compound, we have also investigated the possibility to include an additional isotropic exchange contribution (J) to the spin-spin interaction.

On the one hand, we have exploited low-field specific-heat measurements (a sensitive probe of small gaps arising from exchange interactions) to exclude a significant, ferromagnetic value of J. In zero-field, this is a sensitive probe of the gap arising from exchange interaction. Indeed, we note from Fig. S10 below that $J = -0.1$ cm^{-1} is no longer compatible with the data, while $J = 0$ provides a better fit.

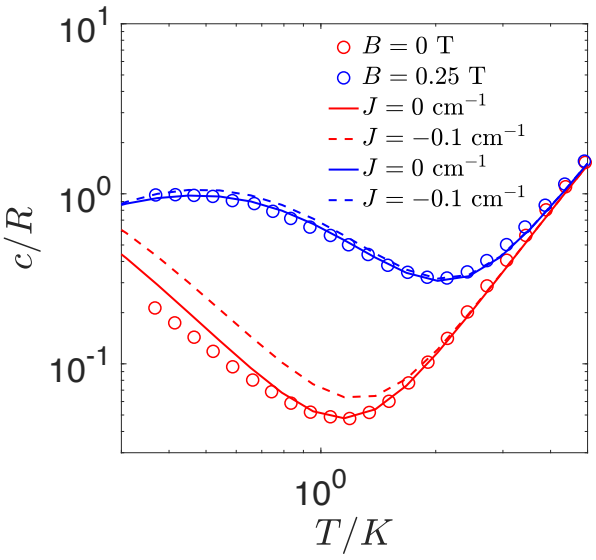

Figure S10. Low-field specific heat vs. temperature on **1**: simulated without (continuous line) or with (dashed) a ferromagnetic isotropic exchange contribution $J = -0.1$ cm^{-1}.

On the other hand, CW-EPR measurements rule out a significant anti-ferromagnetic exchange interaction, as evidenced by the simulations reported in Fig. S11, where we see that J = 0.1 cm^{-1} already worsen the fit (compared to J=0) and J = 0.15 cm^{-1} is clearly out of the tolerable range.

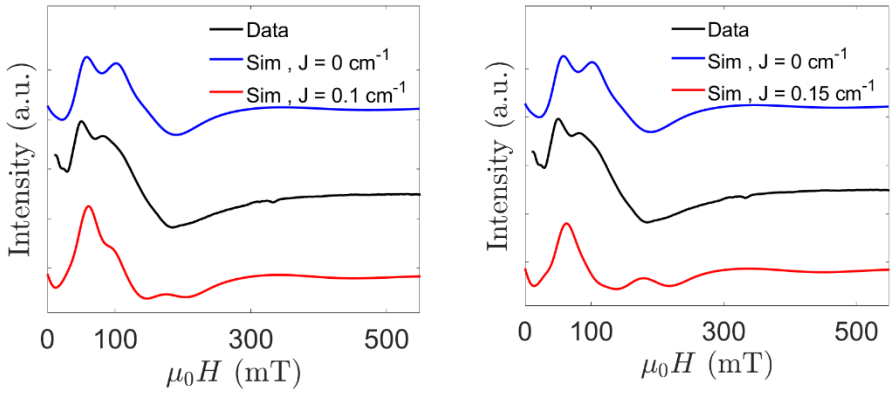

Figure S11. CW-EPR spectra (black lines) on **1**, simulated with (red) or without (blue) an anti-ferromagnetic isotropic exchange contribution.

Since this isotropic exchange interaction only provides a small renormalization of the parameters (without influencing our conclusions), we neglect it for sake of simplicity.

4.5 Pulse EPR experiments on [ErCeEr]

These experiments were aimed to show the possibility of coherently manipulating the states of the trimer and to provide estimates of the coherence T_2 and spin relaxation T_1 time scales, even under non-optimal conditions.

As mentioned above, these measurements were performed on a frozen solution, to reach sufficiently long T_M values while keeping measurably signals. Figure S12 shows a comparison of the cw-EPR spectra measured, at T = 4.5 K, on the frozen solution and on a polycrystalline sample. As expected, the latter shows somewhat broader features and some influence of intermolecular spin-spin interactions, which fully account for the differences between the two spectra. This comparison supports the stability of the [ErCeEr] molecular structure in solution.

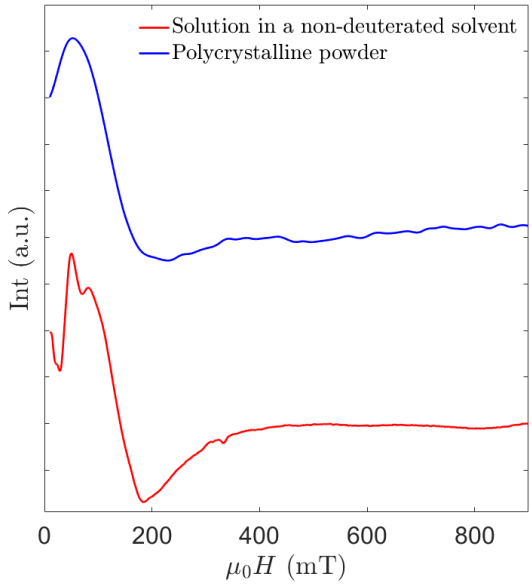

Figure S12. X-band cw-EPR spectra of [ErCeEr] measured on a polycrystalline sample (top panel) and on a frozen solution in 1:1 MeOH/EtOH (bottom panel) at T = 4.5 K.

Using a Hahn echo pulse sequence ($\pi/2 - \tau - \pi - \tau -$ echo), we recorded the amplitude of the spin echo (ESE) as a function of magnetic field for a fixed pulse separation τ = 120 ns. Results are shown in Fig. S12. The observation of an echo-induced spectrum in a magnetic field region spanning most of the transitions accessible at this frequency (9.8 GHz), suggests that all relevant spin states can be coherently manipulated.

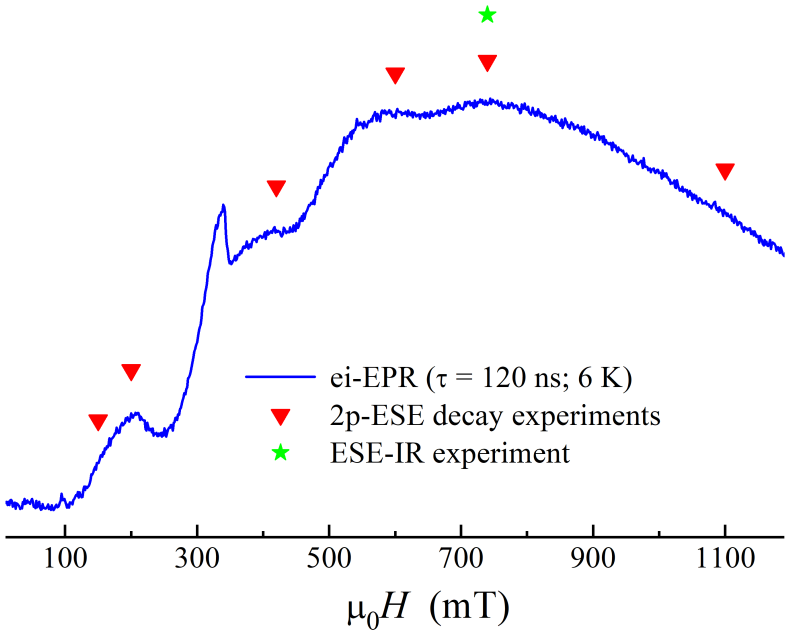

Figure S13. X-band echo-induced EPR spectrum of [ErCeEr] measured on a frozen solution in 1:1 MeOH/EtOH at *T* = 6 K (solid line). The dots show the magnetic fields at which 2-pulse and inversion recovery time-dependent experiments were recorded, from which spin coherence T_2 and spin-relaxation T_1 times, respectively, are obtained.

At low fields, the decay with τ of the ESE signals (Fig. S14) shows a modulation that is characteristic of the coupling to nuclear spins, and which accounts for the drop in the ei-induced spectrum that is observed below 400 mT (Fig. S13). In addition, the decays show a non-exponential dependence, likely associated with the still non-negligible influence of intermolecular couplings, thus of spin diffusion phenomena, in a relatively concentrated solution. Fits to a double exponential decay, with two components of comparable amplitudes but different T_2, provide a reasonably good account of these data. The data reported in the main text, with $T_2 \approx 0.5$ μs and nearly independent of magnetic field, correspond to the slower decaying component, which eventually determines the characteristic time for which coherence vanishes at each field. [18]

[18] Bader, K. et al.; *Chem. Commun.* **2016** *52*, 3623-3626.

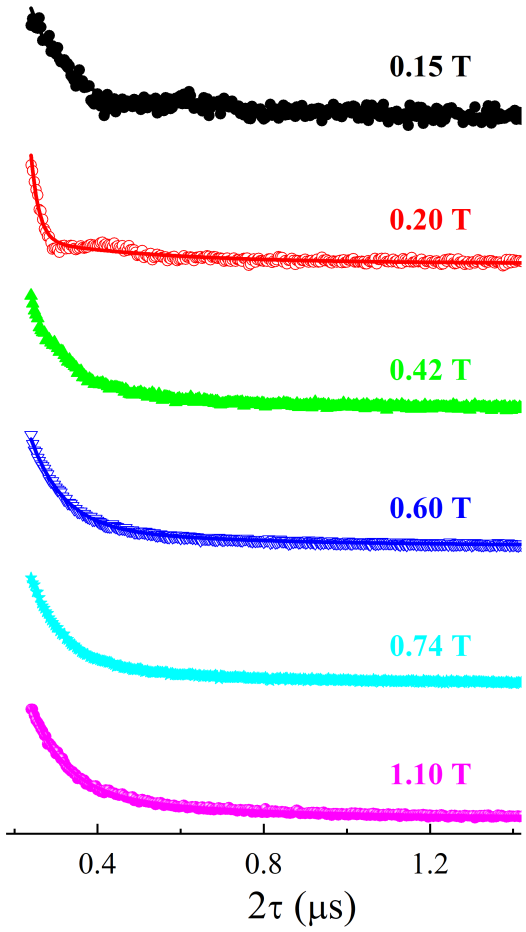

Figure S14. Decay of the ESE measured with a two-pulse sequence ($\pi/2 - \tau - \pi -$ ESE) at T = 6 K and the indicated magnetic fields. The solid lines are least-squares fits to the sum of two exponential decays.

The spin relaxation time was estimated, at 740 mT, by measuring the population recovery after a π pulse. The results are shown in Fig. S15. As it happens with the 2-pulse ESE decays, the time evolution of the spin recovery signal is not exponential but can be fitted by the superposition of two exponential decays. The longest T_1 is of order 4.3 μs.

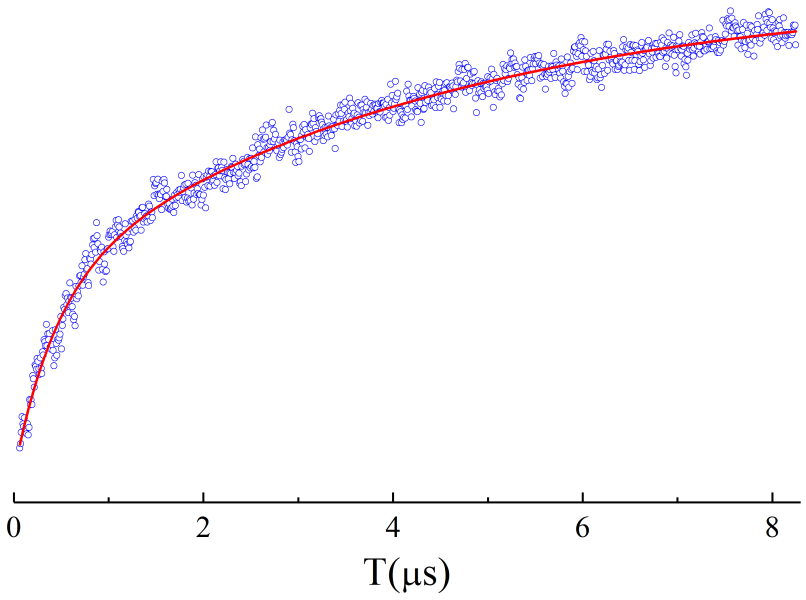

Figure S15. Inversion recovery measured using a $\pi - T - \pi/2 - \tau - \pi - \tau -$ ESE pulse sequence with fixed τ = 220 ns at T = 6 K and at a 740 mT magnetic field. The solid line is a least-squares fit to the sum of two exponential decays with characteristic spin-relaxation times $T_1^{(1)}$ = 0.44(3) μs and $T_1^{(2)}$ = 4.3(2) μs.

5. NUMERICAL SIMULATIONS

5.1 Level diagrams

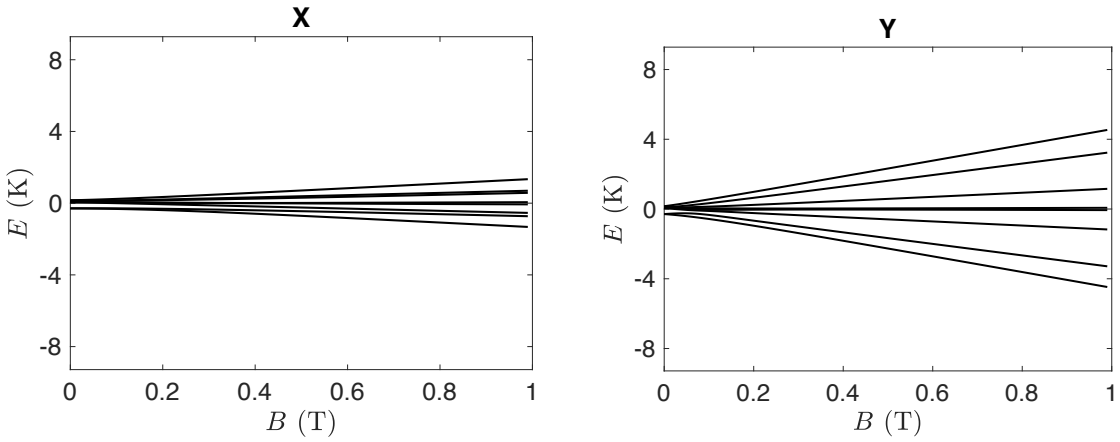

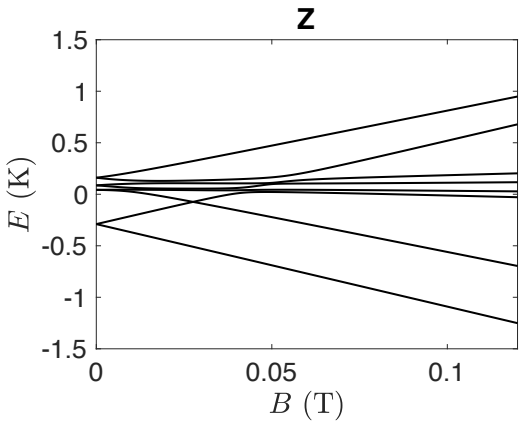

Figure S16. Energy level diagrams for **1**, calculated with the parameters derived from the experimental characterization above and for different direction of the static field *B*. A zoom at low field along *z* is reported.

5.2 Simulation of the three-qubit phase flip repetition code

The whole pulse sequence lasts 55 ns, with independent gates performed in parallel in order to shorten the total duration and therefore improve the performance of the code. In Fig. S17 we report a schematic representation of the pulse sequence of the decoding block, which includes single-qubit gates [$R_y(-\pi/2)$], two-qubit gates ($cNOTs$) and the three-qubit error correcting gate (Toffoli). The encoding gates (not displayed in Fig. S17) are implemented in the same way as $cNOTs$ and rotations of the decoding block.

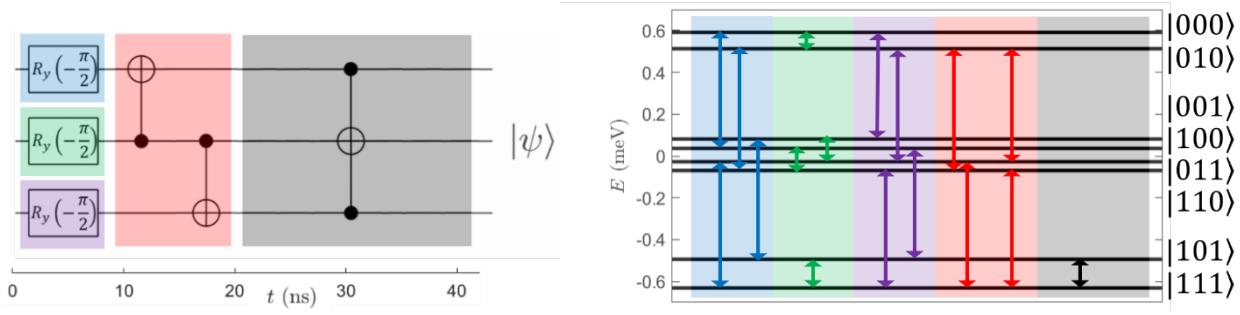

Figure S17. Left panel: decoding block of the TQC highlighting the approximate duration of each set of gates. The three $R_y(-\pi/2)$ gates are performed in parallel with an overall duration of 8.04 ns (shaded areas with different colors refer to different qubits); the two cNOT gates are performed in sequence with a total duration of 11.23 ns (red shaded area); the Toffoli gate is by far the longest of the gates of the TQC, with a duration of 16.08 ns (grey shaded area). Right panel: scheme of the transitions that we need to excite performing each gate, with the color code being the same as in the left panel for better readability. The energy gaps between the levels are obtained with a static field *B* = 1 T along *z*.

5.3 Fidelity of the TQC

We report below the derivation of the analytical expression for the fidelity after an ideal implementation of the three-qubit code[19].

We consider the initial encoded state $|\psi\rangle = \alpha|000\rangle + \beta|111\rangle$, corresponding to the density matrix $\rho = |\psi\rangle\langle\psi|$. If the error occurs with probability p on any of the three qubits, we can write the density matrix after the error as:

$$\rho_{err} = (1 - 3p^2(1-p) - 3p(1-p)^2 - p^3)\,\rho + \tag{1}$$

$$+p(1-p)^2 \sum_{i=1}^{3} Z_i\,\rho\,Z_i +$$

$$+p^2(1-p) \sum_{\substack{i,j=1 \\ i\neq j}}^{3} Z_iZ_j\,\rho\,Z_iZ_j +$$

$$+p^3 Z_1Z_2Z_3\,\rho\,Z_1Z_2Z_3$$

Where $Z_i = 2S_{z,i}$ represents the phase error operator on the i^{th} qubit. This is a mixture of states subject to no errors (first line), a Z error on a single qubit (second line), Z erroras on two or three qubits (third and fourth lines). After the error correction, the one qubit error part of ρ_{err} which is proportional to $p(1-p)^2$, is restored to the correct value ρ (on the logical qubit). On the other hand, the two- and three-qubit error parts of ρ_{err} (proportional to $p^2(1-p)$ and p^3, respectively) are not corrected by the code, resulting in a phase-flip on the logical qubit. Therefore, the final fidelity on the logical qubit is given by:

$$\mathcal{F}^2 = \langle\psi|\rho_{err}|\psi\rangle = (1 - 3p^2(1-p) - p^3)\langle\psi|\rho|\psi\rangle + (3p^2(1-p) + p^3)\langle\psi|\rho_{err,2,3}|\psi\rangle =$$

$$= 1 - 3p^2(1-p) - p^3 + (p^2(1-p) + p^3)4|\mathrm{Re}\,(\alpha^*\beta)|^2 = \tag{2}$$

$$= 1 - (3p^2(1-p) + p^3)[1 - 4|\mathrm{Re}\,(\alpha^*\beta)|^2]$$

where we have exploited $\langle\psi|\rho|\psi\rangle = 1$ and $\langle\psi|\rho_{err,2,3}|\psi\rangle = |\alpha\beta^* + \alpha^*\beta|^2 = 4|\mathrm{Re}\,(\alpha^*\beta)|^2$.

This leads to:

$$\mathcal{E} = 1 - \mathcal{F}^2 = (3p^2(1-p) + p^3)[1 - 4|\mathrm{Re}\,(\alpha^*\beta)|^2] \tag{3}$$

Note that the single-qubit error probability p is directly linked to the time τ/T_2 used in the main text by the following relation:

[19] Nielsen, M. A.; Chuang, I. L.; *Quantum Computation and Quantum Information*; Cambridge University Press: Cambridge, England, (2000).

$$p = \frac{1 - e^{-\tau/T_2}}{2} \tag{4}$$

5.4 Text-book implementation

We have tested the correct implementation of the code by considering the action of an instantaneous phase error after the encoding step. These errors occur on each qubit with probability p, as in equation (1). As stated in the text, we initialize the logical qubit in $|\psi\rangle_L = (|0\rangle + i|1\rangle)/\sqrt{2}$, which is the most error-prone states. Indeed, as computed analytically in equation (3), the residual error $\mathcal{E}$ (i.e. the amount of error not corrected by the TQC) for a qubit subject to the phase damping channel maximized for purely imaginary $\alpha^*\beta$. The results of these simulations are shown in Fig. S18.

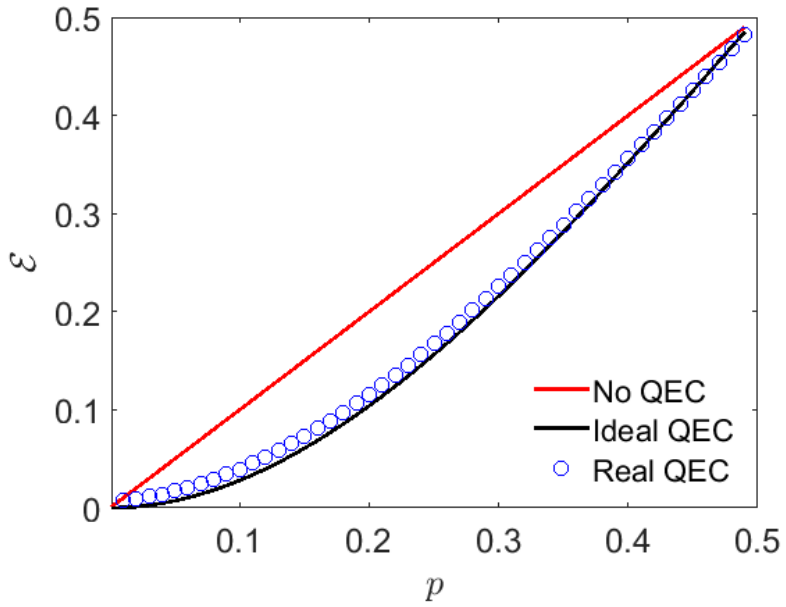

Figure S18. Residual error after implementation of the QEC code as a function of the probability p of an error occurring on any of the three qubits immediately after encoding. Simulations (blue circles) are compared to the ideal performance of the TQC (red line) and with the qubit on which no QEC has been applied (black line).

5.5 Continuous pure dephasing

By including the effect of pure dephasing induced by the coherence time T_2 in the Liouville-von Neumann equation we can estimate the harmful effect of the finite time T_{QEC} in which the TQC is implemented. In the following, we show the final error $\mathcal{E}$ as a function of the memory time τ in units of T_2, whereas the gain $\mathcal{R}$ is shown in the main text.

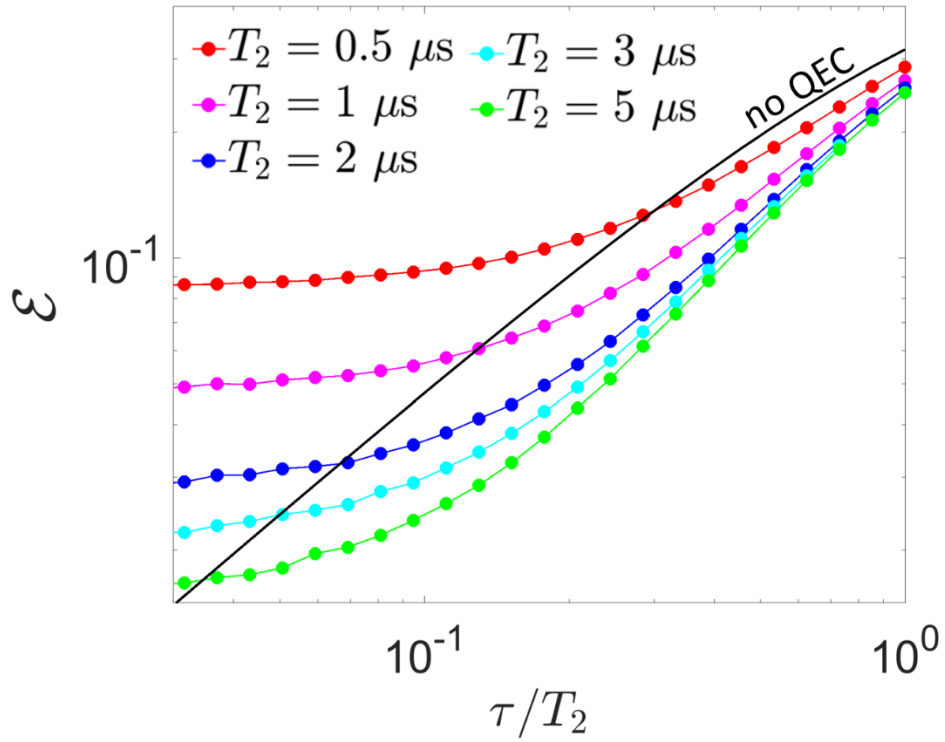

Figure S19. Final error $\mathcal{E}$ as a function of τ/T_2 for five different values of T_2. Solid black line represents $\mathcal{E}$ for an isolated qubit undergoing pure dephasing.

Figure S19 shows how the finite duration of the code T_{QEC} influences the performance of the code, yielding a plateau at short τ/T_2. This happens because phase errors occurred during encoding and decoding are not corrected by the code. However, this effect is reduced by increasing T_2 and for all the values of T_2, our code outperforms the isolated qubit at a certain crossover time, approaching the ideal performance of the TQC at higher τ/T_2.

5.6 Performance of the scheme in less optimal experimental conditions

It is finally useful to examine the performance of our scheme in less optimal experimental conditions. In particular, we consider in Fig. S20 a lower and slightly tilted magnetic field. Both changes yield a reduction in the factorization of the eigenstates. Nevertheless, the gain compared to an uncorrected qubit is still significant, only slightly worsened compared to the simulations at 1 T and $\theta = 0$.

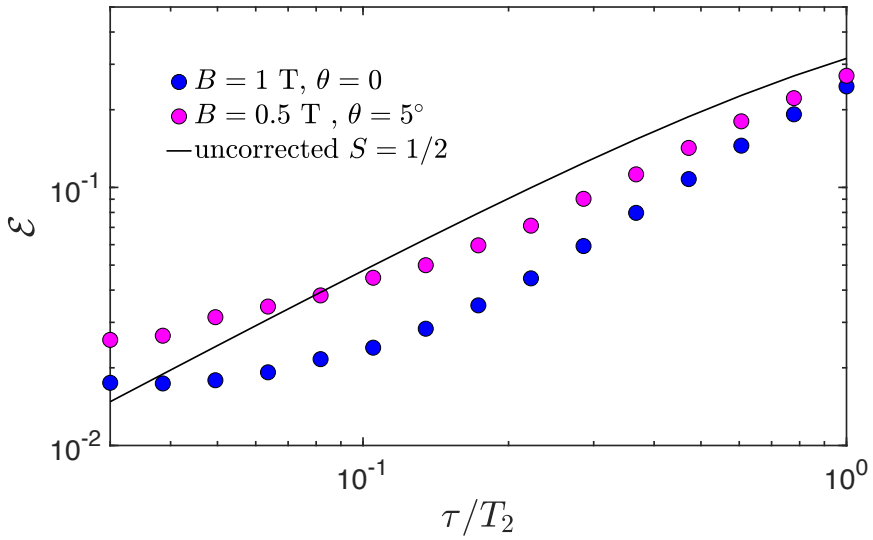

Figure S20. Simulation (using T_2 = 5 μs) of the final error $\mathcal{E}$ as a function of τ/T_2 with a smaller and slightly tilted external field (pink circles), compared with the case reported in the text (blue points).

In addition, it is interesting to investigate a possible alternative to improve T_2, while still keeping high fidelities. Indeed, shorter manipulation times could be achieved by the use of stronger oscillating fields B_1, e.g. with on-chip superconducting resonators, which will probably be needed to perform any proof-of-concept realization[20]. A comparison between the final error obtained by doubling either T_2 or B_1 is reported in Fig. S21, showing similar results. The error is only slightly larger in the simulations using $B_1 = 100$ G, because shorter pulses are broader in frequency and hence induce a slightly larger leakage in some transitions.

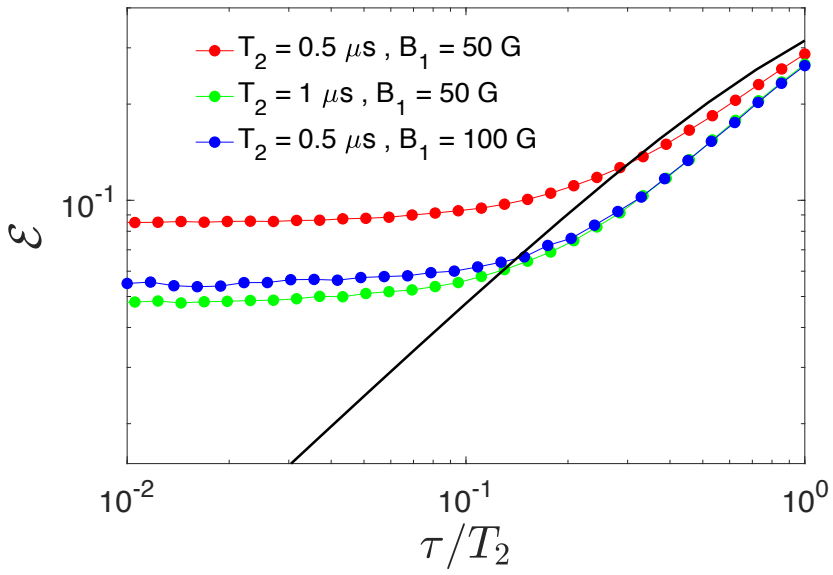

Figure S21. Simulation of the final error $\mathcal{E}$ as a function of τ/T_2, comparing the decrease of T_2 with the increase of the oscillating field amplitude B_1.

[20] M. D. Jenkins et al., Dalton Trans. 2016, **45**, 16682.